Journal of Power Sources 525 (2022) 231079

Contents lists available at ScienceDirect

Journal of Power Sources

journal homepage: www.elsevier.com/locate/jpowsour

Stretchable self-charging energy integrated device of high storage efficiency

O. Hyeon Kwon [a], Jun Ryu [b], Ji Hye Lee [a], Hee Woong Kim [a], Jung Sang Cho [c], Sang Mun Jeong [d,***], Dong-Won Kang [e,**], Jae-Kwang Kim [a,*]

[a] *Department of Energy Convergence Engineering, Cheongju University, Cheongju, Chungbuk, 28503, Republic of Korea*
[b] *School of Smart City, Chung-Ang University, Seoul, 06974, Republic of Korea*
[c] *Department of Engineering Chemistry, Chungbuk National University, Chungbuk, 28644, Republic of Korea*
[d] *Department of Chemical Engineering, Chungbuk National University, 1 Chungdae-ro, Seowon-gu, Cheongju, Chungbuk, 28644, Republic of Korea*
[e] *School of Energy Systems Engineering, Chung-Ang University, Seoul, 06974, Republic of Korea*

HIGHLIGHTS

- A stretchable SRB-integrated energy device is fabricated.
- A polymer–metal-island non-woven common substrate for the SRB is presented.
- The stretchable integrated SRB could effectively offers an elastic response.
- The PSE of the integrated SRB energy device was 13.3%.
- The SRB device achieved an 89.34% capacity retention after 100 cycles.

GRAPHICAL ABSTRACT

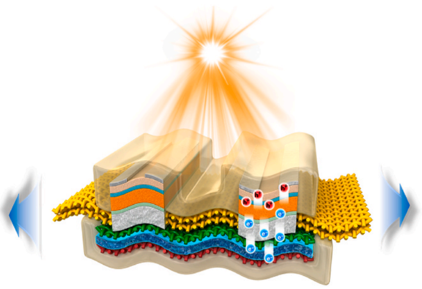

ARTICLE INFO

Keywords:
Integrated energy device
Self-charging
Solar-rechargeable battery module
Metal-island common substrate
Self-energy storage efficiency

ABSTRACT

Integrated energy devices consisting of solar cells and rechargeable batteries are in great demand in wearable electronics and low-energy-density applications in fields such as healthcare. However, developing energy-efficient stretchable energy systems is very difficult due to numerous technical limitations. Herein, a stretchable solar module/rechargeable lithium-ion battery-integrated energy device using a zig-zag truncated electrode for energy storage, nano-sized electrode materials and a polymer–metal-island non-woven common substrate for the integration device is presented. This new stretchable device is portable, has a high operation potential (up to 1.8 V), a long life, high self-charging efficiency, and a high rate-capability. Its self-power conversion/storage efficiency is unprecedented at 13.3%. Additionally, an 89.34% retention capacity can be obtained after 100 cycles, and a surprisingly low-capacity decay of 5.7% in the 30% stretched state is observed. The device's stable performance under various current density and stretching conditions paves the way for the development of highly stretchable integrated energy systems.

---

* Corresponding author.
** Corresponding author.
*** Corresponding author.
E-mail addresses: smjeong@cbnu.ac.kr (S.M. Jeong), kangdwn@cau.ac.kr (D.-W. Kang), jaekwang@cju.ac.kr (J.-K. Kim).

https://doi.org/10.1016/j.jpowsour.2022.231079
Received 15 September 2021; Received in revised form 9 January 2022; Accepted 24 January 2022

1. Introduction

As the number and seriousness of environmental problems continue to increase due to the massive consumption of fossil fuels, the development of eco-friendly renewable energy has garnered much focus. Solar energy is an energy source that can replace fossil fuel energy to provide pollution-free and unlimited clean energy [1,2]. Most importantly, light emitted from the sun can be converted into electrical energy by the formation of excitons. The electricity generated by a solar cell has improved efficiency from being linked to an energy storage system consisting of a rechargeable battery. A rechargeable battery capable of storing such electrical energy and directly converting chemical energy into reversible energy of electrical energy can be hybridized with a photocell [3,4]. However, each device has the disadvantage of highly complex components and excess packaging, weight, and costs. Moreover, mobile electronic devices, such as cell-phones, sensors, and healthcare devices, always demand wired charging of rechargeable batteries that supply power. Therefore, it is important to develop an integrated solar cell-rechargeable battery (SRB) in one device to decrease packaging and improve weight, portability, and efficiency [5–12]. The integrated SRB provides convenience to users by eliminating the need for wired charging and makes it possible for the device to be used semi-permanently.

In recent years, along with the increase in the use of wearable devices, much research and many technical developments in flexible and stretchable devices have progressed [13–16]. Flexible and stretchable electronic devices, which can be easily attached to the skin, have been in high demand mainly because of their enhanced biomonitoring uses. Thus far, several electronic circuits, light emitters, sensors, actuators, and power sources have been reported. For example, submicron-thick organic electrical circuits that can be directly attached onto human skin for ultra-comfortable monitoring have been tested. To develop stretchable devices, it is necessary to design a stretchable structure using a deformable material with excellent mechanical robustness and electrochemical properties, which may lead to the development of new smart textiles, robot skins, and stretchable electronic devices [17]. Accordingly, power supplies of wearable devices, including stretchable devices, have gained great attention. SRB converts electrical energy into chemical energy appropriate for a storage device and uses electrical energy when needed because it does not require a separate power supply and charges batteries by sunlight [18–23]. In addition, the hybridized equipment with added elasticity has a higher structural utilization than the conventional rigid SRB and is suitable for interfaces and can reduce transmission loss, thereby increasing energy density [24,25]. Until now, a stretchable SRB has not been reported in any other field, as it is very challenging to develop.

In this study, a solar module was fabricated on a stretchable common substrate in the form of a metal foil island to give stretchability to the rigid solar module, and the electrode of the battery part was designed in a zig-zag truncated form for the stretchable SRB to ensure stretchability. In addition, non-woven PVdF-HFP film was prepared for the common substrate and was positioned between the solar cell and rechargeable battery and stretchable gel polymer electrolyte (GPE) [26]. It was bonded to the metal foil island, which is connected to the anode of the energy storage part and also the silicon-based photovoltaic module of the energy conversion part to allow movement during stretching. The photovoltaic module was assembled on the Cu metal foil island in the non-woven PVdF-HFP common film, which was bonded to the zig-zag truncated anode current collector of the battery. This allowed the collector to directly collect photo-generated electrons in the battery without wiring to reduce transmission loss and increase energy density. Moreover, the electrodes demonstrated high stability and conductivity in a deformed zig-zag structure. Based on this unique architecture, the self-power conversion/storage efficiency of the integrated device is 13.3%, which is unprecedented value in this field. Additionally, the stretchable energy device using the stretchable zig-zag truncated $Li_4Ti_5O_{12}$ anode and zig-zag truncated $LiFePO_4$ cathode exhibited the remarkable retention capacity of 89.34% after 100 cycles. Furthermore, an impressive low-capacity decay of 5.7% was realized in the 30% stretched state. The mechanism for this unique stretchable SRB and the superior electrochemical properties of the photovoltaic module and stretchable rechargeable battery were investigated in detail.

2. Experimental

2.1. Materials

An $LiFePO_4$ (LFP) cathode material for the stretchable battery was prepared using a coprecipitation process. Fe-acetate[Fe-$(COO)_2$], $NH_4H_2PO_4$, and Li-acetate(Li–CH_3COO) were added to tetraethylene glycol (TTEG) at a molar ratio of 1:1:1. The solution was heated slowly to 200 °C and then rapidly heated to 320 °C in 10-min intervals. The temperature of the mixed solution was kept at 320 °C for 16 h in a round bottom flask attached to a reflux condenser. To remove the TTEG and organic compounds, the solution produced above was washed several times with acetone, methanol, and ethanol. At this time, the generated particles were separated by filtration with a ceramic membrane funnel and dried in a vacuum oven at 150 °C for 24 h.

$Li_4Ti_5O_{12}$ (LTO), an anode material for the stretchable battery, was synthesized by a solid–solid complex reaction using fine Li_2CO_3 and TiO_2 anatase as starting materials. The molar ratio of Li:Ti was 4:5. The powder was put into the machine and mixed according to the above ratio. The stirring speed was set to 3000 rpm, and the operating time was 1 h. The powder was sintered after mixing at a temperature of 850 °C for 10 h. After heat treatment, the LTO powder was agglomerated without strong bonding. The agglomerated LTO was crushed using a mortar and pestle.

The cathode (anode) was fabricated by blending LFP and LTO with carbon black (TIMCAL) and polyvinylidene fluoride (PVdF) (Mw = 534,000, Sigma-Aldrich) at a weight ratio of 9:0.6:0.4, respectively. The LFP and LTO electrodes were made uniform by making structural changes in a zig-zag truncated form for stretchability with 9.0 mg cm^{-2} loading.

2.2. Preparation of gel polymer electrolyte

The PVdF-HFP-based gel polymer electrolyte was prepared using an electrospinning method to ensure stretchability. Briefly, 16 wt% of PVdF-HFP was dissolved in acetone and dimethylacetamide (DMAc) (7:3, v/v). The electrospinning parameters were as follows: the applied voltage was 18 kV, the distance between the tip of the needle and collector was 15 cm, the needle size was 0.31 mm, the solution feed rate was 2.0 mL h^{-1}, and the collector drum rotation speed was 200 rpm. To prepare the gel polymer electrolyte (GPE), the electrospun membrane was impregnated with 1.2 M $LiPF_6$ in ethylene carbonate (EC): dimethyl carbonate (DMC) at a 1:1 vol%.

The chemical composition of the prepared samples was characterized by Fourier transform infrared (FT-IR) spectroscopy (IFS 66/S Bruker Optik GmbH, Germany). The X-ray photoelectron spectroscopes (XPS) of materials were obtained with an XP spectrometer (PHI 5500, Physical Electronics, Inc., ULVAC-PHI, USA/Japan). Al K_α irradiation (1485.6 eV) was used as the X-ray source at an anode voltage of 13.8 kV. The morphology and elemental mapping were examined by scanning electron microscopy (SEM) and energy-dispersive X-ray spectroscopy (EDS) (JSM-7610F, JEOL).

2.3. Fabrication of stretchable photo-rechargeable battery

For efficient photo-charging of the battery, monocrystalline silicon (Si)-based solar modules (40 mm × 32 mm, for 4 V, 60 mA, and 8 mm × 4 mm, for 1 V, 5 mA) were prepared based on the YKSM models from the YOLK corporation. Photo-rechargeable batteries were fabricated in an

Ar-filled glove box. Fig. S1 presents fabrication process of integrated SRB. The electrospun PVDF-HFP polymer membrane as a common substrate was used to give the rigid solar modules elasticity.

On the polydimethylsiloxane (PDMS) film, the LFP zig-zag truncated cathode, gel polymer electrolyte, LTO zig-zag truncated anode, stretchable non-woven polymer–metal-island composite common substrate, and Si solar module were assembled in this order. The Si solar module was attached onto the metal common island (Cu foil) in the middle of the PVdF-HFP common substrate using silver paste (CANS). Here, the positive terminal of the solar modules came out separately to be connected with one of the batteries. The prepared solar module/metal-island common substrate was connected to the current collector of the negative electrode in back side. Welding was required to attach the Cu foil of the common substrate to the current collector (Cu foil) of the zig-zag LTO's negative terminal to suppress possible contact resistance as much as possible. After that, the PVDF-HFP-based gel polymer electrolyte stacked on the LTO zig-zag truncated anode and the zig-zag LFP cathode was placed onto PVDF-HFP-based gel polymer electrolyte. Finally, the PDMS was covered the SRB and sealed with polyolefin elastomer (POE) by thermocompression binding. The top surface of the photo-rechargeable battery was protected by coating the PDMS layer to obtain a stretchable integrated system.

2.4. Electrochemical characterization of solar modules and photo-rechargeable battery

The photocurrent–voltage (I–V) curve of a solar module under illumination can be used to evaluate the power conversion efficiency (PCE) using the following equation:

$$PCE\left(\%\right) = \frac{P_{out}}{P_{in}} = \frac{I_{SC}V_{OC}FF}{P_{in}}$$

where P_{in} and P_{out} are the input and output power, respectively, for the solar module, FF is fill factor, and I_{SC} and V_{OC} are the short-circuit photocurrent and open-circuit voltage, respectively.

Electrochemical characterization of the stretchable batteries and integrated solar module-rechargeable battery device was performed using an automatic galvanostatic charge–discharge unit and a WBCS3000 battery cycler. The stretchable LFP-LTO zig-zag full-cell was assembled using GPE as a separator and electrolyte. The area of LFP electrode was 10 cm^2 and the mass loading was 9.0 mg cm^{-2}. Electrochemical impedance spectra were obtained through electrochemical impedance spectroscopy (EIS, ZIVE SP1) over a frequency range of 1 MHz–10 mHz at a potential of 10 mV. The stretchable LFP-LTO full-cells and SRB were operated with a working voltage range of 1.0–2.5 V at different current densities.

3. Results and discussion

A schematic diagram of the stretchable SRB assembled based on the zig-zag structure is shown in Fig. 1a. The common substrate between the photovoltaic module and rechargeable battery was prepared using an electrospinning process, as shown Fig. S2. The common substrate was formed with Cu foil as metal islands, and the solar module and rechargeable battery were assembled on opposite sides. The anode of the PV module directly comes into contact with and shares the lithium-ion battery (LIB) via the Cu foil, and the cathode is connected through a wired connection. Electrons/holes generated in the PV module are separated and flowed into the anode/cathode of the LIB, respectively. In the integrated SRB device, when the photocurrent flows through the circuit due to the energy conversion from the solar module, the generated electrons pass through the common substrate and are stored in the anode of the battery. LFP is oxidized at the cathode with lithium-ion extraction during the charging process. Then, the LTO is reduced at the anode through the lithium-ion insertion process. The stored energy is released to an external load when lithium ions move back from the anode to the cathode via the discharging process of the battery part.

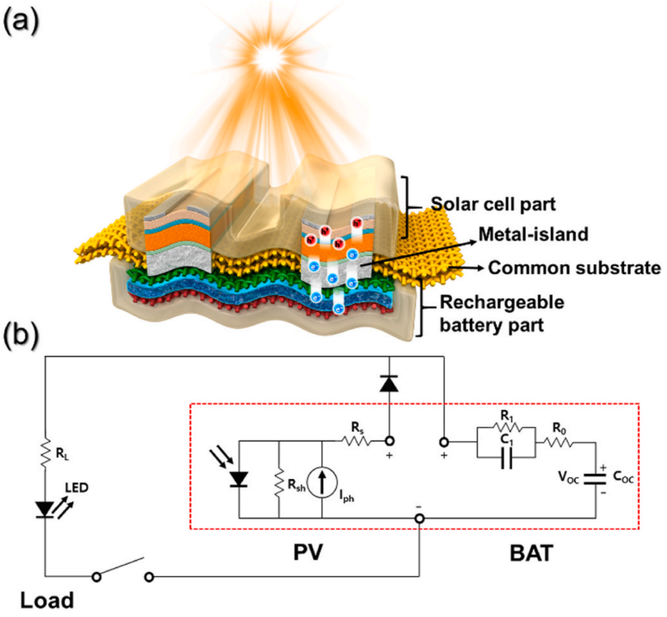

Fig. 1. The fabricated stretchable SRB device structure and its equivalent circuit diagram. (a) The SRB schematic diagram and (b) an equivalent circuit for modeling the SRB device.

In existing flexible batteries and SRBs, the deterioration in performance due to deformation is one of the problems with the system structure. However, if physical deformation is applied to a hard electrode, such as metal, the performance of the battery is greatly degraded because it cannot withstand the peeling and cracking of the electrode slurry material caused by the current collector. Since the metal current collector has a low elasticity, it is important to design a flexible electrode with stable electrical performance during deformation. Additionally, a stretchable battery manufactured in an integral form with a PV module has not been announced, and to solve this problem, we designed a zig-zag truncated electrode with high shape stability and electrospun PVdF-HFP as GPE, which has good porosity, good elasticity, and high ionic conductivity. They were used for SRB and integrated with a PV module to enable movement during stretching.

Fig. 1b shows the overall circuit diagram with a light emitting diode (LED) load, and the red dotted line shows the equivalent circuit parts consisting of the PV module and rechargeable battery in the SRB in Fig. 1a. In addition, a rectifying diode was connected between the PV module and battery to prevent undesirable current flow from the battery to the PV module for protection in dark conditions. In a dark condition, the PV module does not generate electricity, and an LED can provide illumination by turning on a switch. This can be made via the discharging mode of the battery. When sufficient light is insolated, the photo-voltage of the PV module increases over the extent of (battery voltage + diode turn on voltage (~0.6 V)). Then, the solar charging mode can begin.

Fig. 2a shows the I–V characteristics of a PV module with and without a rectifying diode that is connected to a stretchable common substrate for SRB. The PV module integrated on a stretchable substrate provides the PV performances of an I_{SC} of 54.35 mA, a V_{OC} of 5.18 V, an FF of 72.37%, and a PCE of 15.91%, which was designed to sufficiently charge our stretchable battery. Our silicon modules are connected in series to provide sufficient charging voltage for stretchable battery. The diode-connected PV module shows a photocurrent curve that can stably supply a current to charge the LTO/LFP LIB with a cut-off range of 1.0–2.5 V. We adjusted the photocurrent output of our PV module by tuning the light insolation intensity to obtain the C-rate characteristic

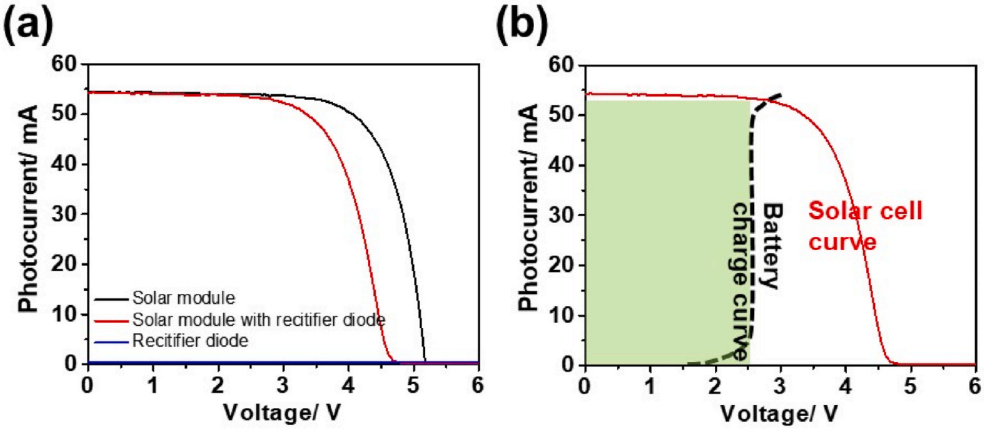

Fig. 2. The stretchable solar module performance and stretchable SRB device operation region (a) I–V properties of the Si solar module for SRB with a rectifier diode under 100 mWcm^{-2}. (b) overlapping I–V curves for the effective self-charging of an integrated energy device.

curve of the battery. Fig. S3 shows the I–V properties of the diode-connected Si solar module used to provide 0.1 (3 Wh m^{-2}) to 5C (150 Wh m^{-2}) for the stretchable battery. As light insolation intensity decreases in general Si-based solar cells, I_{sc} decreases significantly [27]. The diode-connected PV module shows a photocurrent curve that can stably supply a current to obtain a value of 0.1–5 C in the C-rate characteristic curve of the stretchable LTO/LFP battery in the range of 1.0–2.5 V.

To control the efficient self-charging of SRB, the current and voltage of both the solar module and rechargeable battery have to be optimized. The charging curve of the energy storage part (rechargeable battery) overlaps the photocurrent–voltage curve of energy conversion part (solar module) to find the efficient operation region, as demonstrated in Fig. 2b. The green area is the efficient self-charging area range that can supply a stable current. The power is limited to a max of 135 mW cm^{-2}, and the charge potential of the battery is limited to 2.5 V. A charge potential higher than 2.5 V does not guarantee stable charging. To assemble an efficient SRB, cathode and anode materials were selected to appoint 2.5 V (cathode potential-anode potential, Li/Li^{+}), and hence, $LiFePO_4$ (charge potential 4.0 V; Li/Li^{+}) as the cathode and $Li_4Ti_5O_{12}$ (potential 1.5 V; Li/Li^{+}) as the anode were employed for the energy storage part of SRB.

The crystallinity and morphology of the synthesized LFP and LTO nanoparticles were confirmed using XRD and SEM (Fig. S4). Figs. S4a–b shows the XRD patterns of the LFP and LTO samples. All patterns can be indexed as single-phase materials with orthorhombic olivine-type structures and spinel structures with approximately the *Pnma* and *Fd3m* space groups as listed in the x-ray diffraction data file (JCPDS card no. 40–1499 for LFP, and 49–0207 for LTO). In addition, no impurities were found in the LFP or LTO powder, indicating that there were no other peaks found in the main peaks of the LFP and LTO. There was no evidence of crystalline carbon, and no amorphous peaks existed, which indicates that pure LFP and LTO were obtained. From the XRD data, the lattice constants of LFP and LTO were calculated to be $a = 10.45$ Å, $b = 6.11$ Å, $c = 4.74$ Å, and $V = 302.65$ Å^3 for LFP, and $a = b = c = 8.36$ Å and $V = 584.28$ Å^3 for LTO, which are in good agreement with the lattice constants reported for phase-pure LFP and LTO [28–31]. FE-SEM was used to observe the particle surface morphology of the samples. The surface morphology of the LFP and LTO particles are shown in Figs. S4c–d. To check whether the synthesized nano particles were evenly dispersed and whether the sizes and shapes of the particles were similar, the images were observed with a magnification of 10000. LFP had various shapes according to particle aggregation, such as nanorods, spherical particles, and nanoplates, and the sizes of the particles were observed with a particle size distribution of 200–300 nm. LTO particles had a characteristic angular shape, and the average size of the particles was observed to be 250 nm. It was confirmed that relatively uniform particles were evenly distributed in both LTO and LFP, and each particle was slightly agglomerated. The uniform and submicron-sized electrode particles are beneficial for improving the lithium-ion diffusion in the electrode and obtaining a high rate-capability [32,33]. The rate-capacity (or quick charging) of the energy storage part is an important factor that needs to be considered to achieve high self-power conversion/storage efficiency (PSE), because the battery part is fabricated as mono-layer electrodes to allow stretchability via the zig-zag truncated form. The solar module supplies a high photocurrent to the stretchable mono-layer electrode lithium-ion battery for charging of the integrated SRB.

Due to its high energy density, excellent stability, and long cycling characteristics, LFP is known as a highly stable cathode material for high-energy LIBs. LTO materials, which are very safe and have excellent rate stabilities, have also been considered as an LIB anode material. The electrochemical performance of the Li/LFP and Li/LTO half-cells with zig-zag truncated electrodes are shown in Fig. 3. Fig. 3a shows the charge-discharge profiles for stretchable Li/LFP half-cell and shows excellent flat voltage bands at various C-rates. Moreover, the stretchable Li/LTO cell (Fig. 3b) displays the charge-discharge curve as characterized by a flat and extended voltage plateau at around 1.6 V. The superior stretchable LTO cell possess excellent electrochemical properties with a good cycle stability and highly specific capacities of 158.2 mAh g^{-1}(at 0.1C, 0.153 mA cm^{-2}). The discharge capacities of the stretchable LFP cell were 145.4, 139.2, 133.6, 126.1, 102.5 at 0.1C, 0.5C, 1.0C, 2.0C, and 5.0C, respectively, as shown in Fig. 3c. In Fig. 3d, the stretchable LTO cell is shown to have maintained the increasing rate-capability. The discharge capacity of the LTO cell was 157.8 mAh g^{-1} for the first cycle at 0.1C, which faded progressively with the increasing rate before stabilizing to about 155.2 mAh g^{-1} at 0.5C, 153.7 mAh g^{-1} at 1.0C, 149.7 mAh g^{-1} at 2.0C and 137.5mAh g^{-1} at 5.0C. When the current was reversed back to 0.1C for the LFP and LTO cells, the capacity immediately recovered its original value (142.6 mAh g^{-1} for LFP and 156.1 mAh g^{-1} for LTO at 0.1C), demonstrating good reversibility even with high-rate cycling. The potential difference (ΔV) between the average charge and discharge potentials of LFP and LTO, which correspond to the mid-points of the curves, increased with current density. The ΔV increased from 0.06 V for 0.1C to 0.63 V at 5C for LFP cells and from 0.015 V for 0.1C to 0.142 V at 5C for LTO cells. The discharge capacity dropped, and ΔV increased with the increased C-rate because of the limitation in the speed of lithium-ion diffusion at a high current density [34–37]. From the rate capability of each stretchable cell, we can speculate that the LTO material has a higher lithium-ion diffusion speed than LFP. As shown in Fig. 3e, after several cycles, the capacity of the Li/LFP cell decreases slowly to around 127.2 mAh g^{-1}. However, the cell exhibited a coulombic efficiency >99% and a fine cycling performance

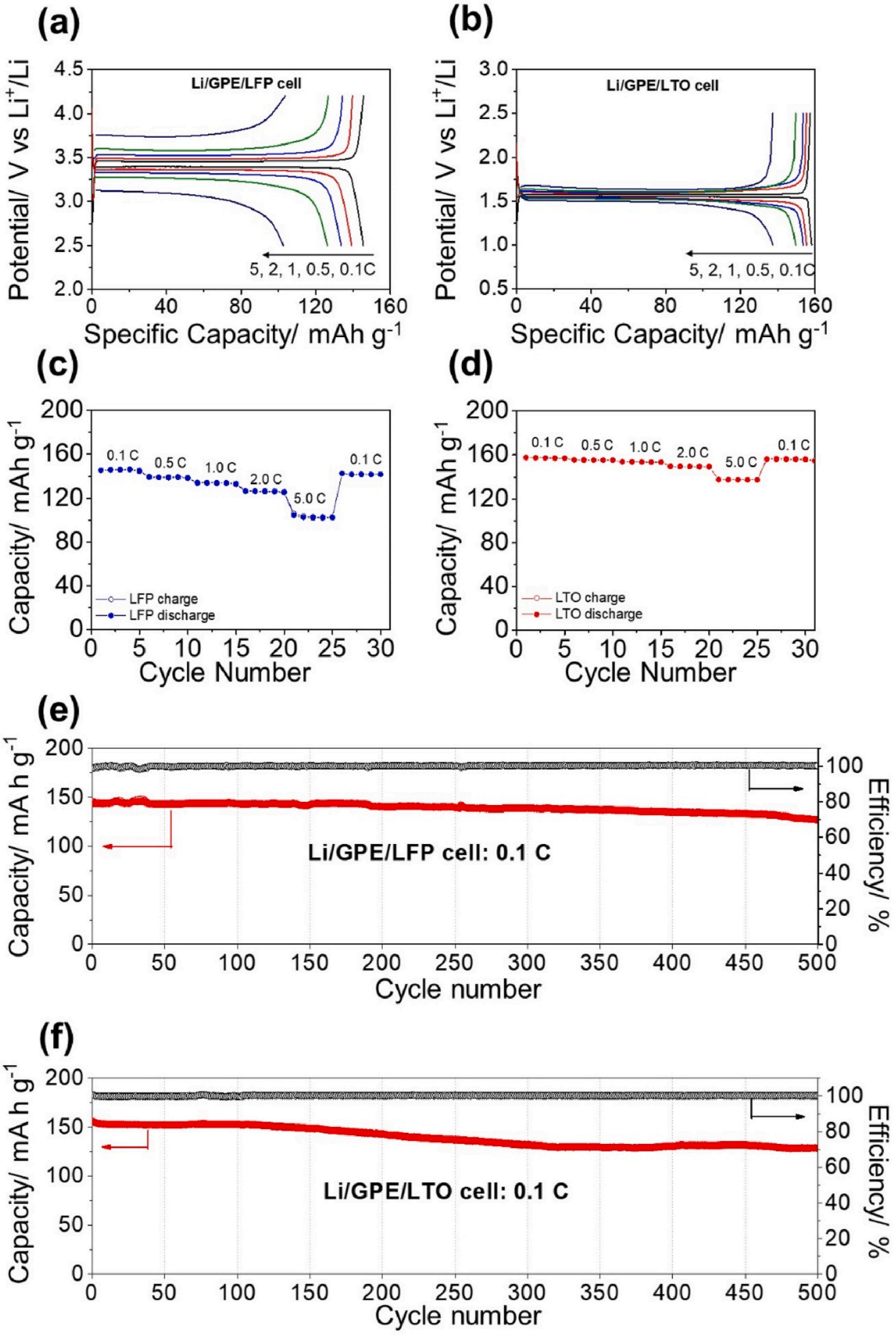

Fig. 3. Electrochemical characterization of stretchable LFP and LTO cells. (a–b) Charge-discharge curves, (c–d) short-cycle rate performance, (e–f) long cycle performance of zig-zag truncated LFP and LTO cells.

of just 500 cycles. Fig. 3f shows the cyclic performance and coulombic efficiency of the stretchable Li/LTO cell; specifically, a capacity of over 128 mAh g^{-1} can be achieved for 500 cycles. The columbic efficiency of the LTO cell for after first cycle was up to 99%, and that for the following cycles increased gradually. A stable coulombic efficiency of ~99.7% could be obtained after 100 cycles. After 500 cycles, the discharge capacity of the LTO cell was 128.7 mAh g^{-1}. Of all the cell profiles, the calculated capacity fade per cycle based on the initial discharge capacity of the cells and the following 500 charge-discharge cycles was very low (0.029% for LFP and 0.034% for LTO).

To prepare a stretchable full-LIB, an anode made of a zig-zag truncated LTO electrode was combined with a zig-zag truncated LFP electrode. The schematic structure of the stretchable full-cell using the zig-zag truncated electrodes is shown in Fig. S5. The charge-discharge curves of the stretchable LTO/GPE/LFP full-cell at 0.1C are shown in Fig. 4a. The process provided a first-charge capacity of 150.2 mAh g^{-1} and a subsequent discharge capacity of 147.0 mAh g^{-1}, resulting in an irreversible capacity loss of 2.1%. The discharge capacity reached 86.5%

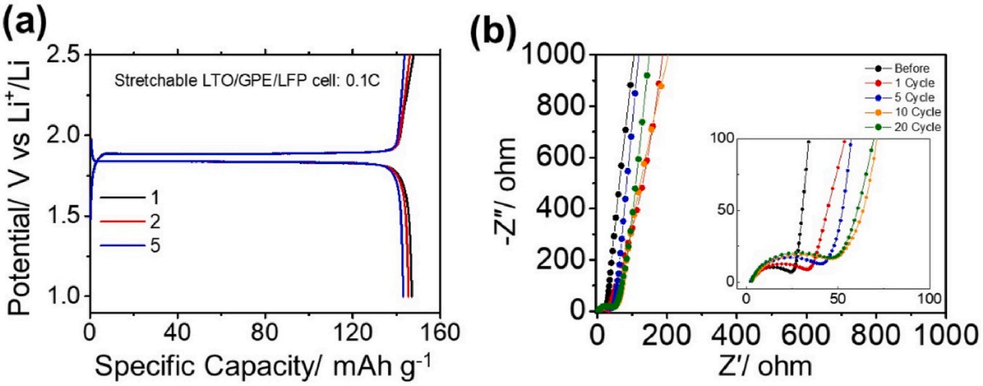

Fig. 4. Electrochemical characterization of stretchable full-cell. (a) Charge-discharge profile and (b) electrochemical interfacial spectra of the stretchable LTO/GPE/LFP full-cell.

of the theoretical capacity of the $LiFePO_4$ material. In addition, in the second and fifth cycles, the discharge capacities were 145.4 mAh g^{-1} and 143.1 mAh g^{-1}, respectively. Their corresponding charge capacities were 147.9 mAh g^{-1} and 144.7 mAh g^{-1}, respectively. Moreover, the coulombic efficiencies in the second and fifth cycles were ~99%. The increased coulombic efficiency with cycling is due to interfacial instabilities and improved penetration of lithium ions. The high capacity and high coulombic efficiency are due to the outstanding ability of the stretchable zig-zag truncated electrodes and the stretchable gel polymer electrolyte, which can rapidly transfer electrons and ions. Optical images of the stretchable gel polymer electrolyte and stretchable LTO/GPE/LFP full-cell connected to a red LED are shown in Fig. S6. Fig. 4b shows the results of the EIS of the stretchable LTO/GPE/LFP full-cell and an equivalent circuit diagram with a scanning frequency range of 1 mHz–1 MHz. The high-frequency region of the semicircle represents the charge transfer impedance, and the low-frequency region of the inclined line is due to the Warburg impedance representing the diffusion of lithium ions. The charge transfer resistance increases up to 10 cycles, but with stabilization, the resistance decreases from 20 cycles. That mean the zig-zag truncated electrodes provide stable electrochemical reaction with gel polymer electrolyte.

The structure diagram of the fabricated self-charging stretchable integrated SRB is shown in Fig. S7. Fig. 5a exhibits the schematics of the stretchable integrated SRB in released and stretched states (0–30%). When the existing metal current collector in the electrode is used, deformation is insufficient during tensioning, resulting in cracks in the active electrode layer. However, it can be stretched without cracking with the designed zig-zag truncated electrode and the elasticity of the PDMS. In addition, the PV module is attached to the stretchable polymer–metal-island common substrate and is not restricted by movements during deformation. Photographs of the integrated SRB confirm the operation and stretchability. Fig. 5b proves the generated current for charging the SRB device using a light source for solar module energy conversion. The stretchable SRB device connected to a LED is shown in Fig. 5c–d at the released and stretched states, respectively. The integrated SRB continuously powered the LED at 30% stretching, and there was no obvious change in the inner-outer shape in the stretched state. To investigate the electrochemical properties of the integrated SRB, a 60 Wh m^{-2} light source was supplied to the solar module, and the rechargeable battery was charged with a self-current storage through a metal-island on a stretchable common substrate (Fig. 5e). After self-charging, the SRB was discharged with various current densities (from 0.1 to 5.0C), and the C-rate was gradually increased from 0.1 to 5.0C. The discharge capacities of the integrated SRB were 145.9, 127.6, 123.8, 113.5 and 88.8 mAh g^{-1} at 0.1, 0.5, 1.0, 2.0, and 5.0 C-rates, respectively. The PSE, a critical property of an integrated energy device, can be calculated using the following equation:

$$PSE(\%) = \frac{P_{discharge}}{P_{insolation}} \times 100\%$$

Here, $P_{insolation}$ is the energy (Wh m^{-2}) of the light source, and $P_{discharge}$ is the discharge energy of the battery part; 60 Wh m^{-2} energy was provided to the solar module, and the integrated rechargeable battery gave 8 Wh m^{-2} in a discharge state of 0.1C. The unprecedented PSE was obtained as 13.3%, which is the better than the reported rigid integrated energy device without stretchability [20,21,38,39]. The rate-capability of the integrated device was estimated in 5 cycles at each step of various current densities (Fig. 5f). The stretchable integrated SRB device allows stable cycling at each current density. Thereafter, the capacity when returned to 0.1C from 5.0C was 140.6 mAh g^{-1}, which showed high reversibility at a high current density. As shown in Fig. 5g, the integrated SRB device initially showed a reversible discharge capacity of 127.64 mAh g^{-1} at a 0.5 C-rate discharge, and after 100 cycles, with a reversible discharge capacity of 114.03 mAh g^{-1}, an excellent capacity retention rate of 89.34% was achieved. The high PSE efficiency is maintained during all cycles and achieved 90% at 100 cycles. The integrated SRB device achieved stable electrochemical performance of up to 30% of the stretched state at 137.6 mAh g^{-1} at 0.1C, but the capacity rapidly decreased to 121.8 mAh g^{-1} at 40% stretching (Fig. S8a). It is speculated due to high contact resistance within the electrode at 40% stretching. The high capacity degradation at 40% stretching When the device returned to 0% stretching, the capacity almost recovered fully, at 145.5 mAh g^{-1}. Therefore, the stretchable integrated SRB device can be operated at up to 30% stretching with a high PSE. The integrated SRB possesses a high discharge capacity (137.1 mAh g^{-1}) and capacity retention (96%) in repeated stretching-release to 100 times, as shown Fig. S8b. Fig. S9 shows that the stretchable integrated SRB devices work well in stretched states (0–30%) without self-discharge during 160 h (Fig. S10). The excellent electrochemical properties of the stretchable integrated energy device attribute to I–V control and low resistance integration design. The developed stretchable integrated SRB is a novel technology and opens a new horizon for stretchable electronic devices and integrated energy devices.

4. Conclusion

To the best of our knowledge, this is the first time a stretchable integrated SRB energy device with discharge potentials reaching up to 1.8 V and with a high efficiency has been reported. Many new scientific technologies, such as zig-zag truncated electrodes for stretchable energy storage part, a polymer–metal-island stretchable common substrate for integrated systems, selected nano-size electrode materials synthesis, and the control of I–V curves for effective self-charging, have been introduced to develop pioneering energy devices. The stretchable integrated SRB could effectively offers an elastic response to large strain

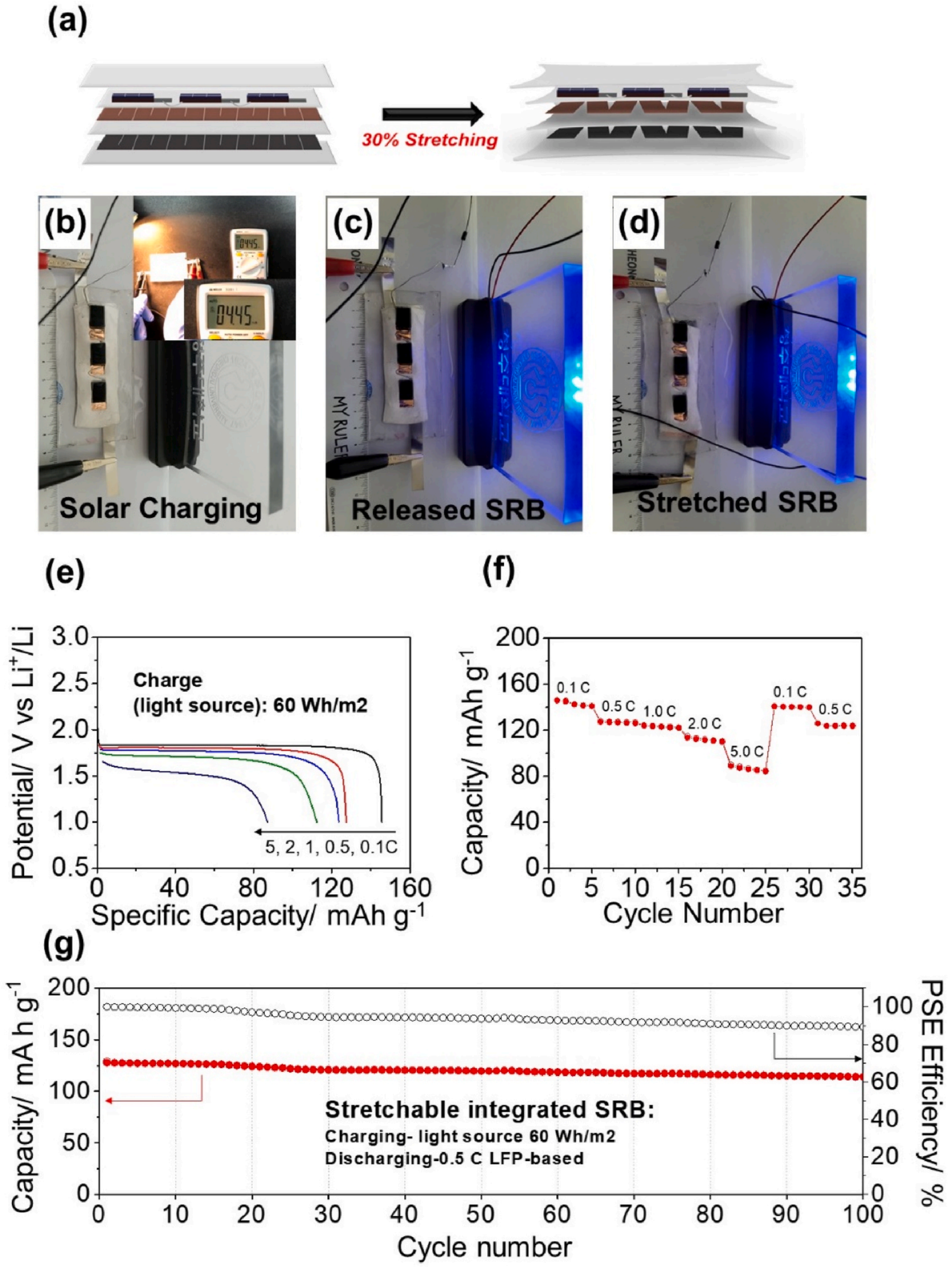

Fig. 5. Schematic of fabrication and characterization of the stretchable SRB energy device. (a) Schematic of the stretchable integrated SRB energy device in released and stretched (30% strain) states. (b) digital photographic image of the SRB energy device with a generated current and its LED light with released state (c) and stretched states (d) of the stretchable SRB energy device. Discharge profiles (e) and rate-performance (f) of the stretchable integrated SRB energy device at different current densities and cycle properties (g) of the stretchable SRB energy device.

deformations of 30% while maintaining good electrochemical performance. The discharge capacities of the integrated SRB were 145.9, 127.6, 123.8, 113.5, and 88.8 mAh g^{-1} at 0.1, 0.5, 1.0, 2.0 and 5.0 C-rates, respectively. The PSE of the integrated SRB energy device was 13.3%, which is the better than any reported integrated energy devices. The SRB device achieved an 89.34% capacity retention that could be sustained after 100 cycles. Additionally, a low-capacity decay of 5.7% in the stretchable integrated device using the zig-zag truncated electrodes at a 30% stretched state was observed. The current stretchable integrated energy device represents an important potential to boost the development and application of stretchable electronics that can be directly worn on the body or be applied to medical devices with semi-permanent use.

CRediT authorship contribution statement

O. Hyeon Kwon: developed the SRB module, performed experiments on the integrated device, analyzed the data and created the figures, wrote and edited the paper. **Jun Ryu:** analyzed the data and created the figures, wrote and edited the paper. **Ji Hye Lee:** helped experiments and contributed to developing the concept. **Jung Sang Cho:** helped experiments and contributed to developing the concept. **Sang Mun Jeong:** plots and oversaw the project. **Dong-Won Kang:** developed the concept of stretchable integrated SRB energy device, wrote and edited the paper. **Jae-Kwang Kim:** developed the concept of stretchable integrated SRB energy device, wrote and edited the paper.

Declaration of competing interest

The authors declare that they have no known competing financial interests or personal relationships that could have appeared to influence the work reported in this paper.

Acknowledgements

This work was supported by the National Research Foundation of Korea (NRF) grant funded by the Korea government (MSIT) (NRF-2021R1A4A2001687).

Appendix A. Supplementary data

Supplementary data to this article can be found online at https://doi.org/10.1016/j.jpowsour.2022.231079.

References

[1] Z. Şen, Solar energy in progress and future research trends, Prog. Energy Combust. Sci. 30 (2004) 367–416, https://doi.org/10.1016/j.pecs.2004.02.004.

[2] A. Fahrenbruch, R. Bube, Fundamentals of Solar Cells: Photovoltaic Solar Energy Conversion, Elsevier, 2012.

[3] K. Jost, G. Dion, Y. Gogotsi, J. Mater, Textile energy storage in perspective, Inside Chem. 2 (2014) 10776–10787, https://doi.org/10.1039/C4TA00203B.

[4] J. Xu, Y. Chen, L. Dai, Efficiently photo-charging lithium-ion battery by perovskite solar cell, Nat. Commun. 6 (2005) 1–7, https://doi.org/10.1038/ncomms9103.

[5] D. Schmidt, M.D. Hager, U.S. Schubert, Photo-rechargeable electric energy storage systems, Adv. Energy Mater. 6 (2016) 1500369, https://doi.org/10.1002/aenm.201500369.

[6] A. Paolella, C. Faure, G. Bertoni, S. Marras, A. Guerfi, A. Darwiche, P. Hovington, B. Commarieu, Z. Wang, M. Prato, Light-assisted delithiation of lithium iron phosphate nanocrystals towards photo-rechargeable lithium ion batteries, Nat. Commun. 8 (2017) 1–10, https://doi.org/10.1038/ncomms14643.

[7] P. Liu, H. Yang, X. Ai, G. Li, X. Gao, A solar rechargeable battery based on polymeric charge storage electrodes, Electrochem. Commun. 16 (2012) 69–72, https://doi.org/10.1016/j.elecom.2011.11.035.

[8] M.M. Lee, J. Teuscher, T. Miyasaka, T.N. Murakami, H.J. Snaith, Efficient hybrid solar cells based on meso-superstructured organometal halide perovskites, Sci 338 (2012) 643–647, https://doi.org/10.1126/science.1228604.

[9] W. Guo, X. Xue, S. Wang, C. Lin, Z.L. Wang, An integrated power pack of dye-sensitized solar cell and Li battery based on double-sided TiO2 nanotube arrays, Nano Lett. 12 (2012) 2520–2523, https://doi.org/10.1021/nl3007159.

[10] Z. Tian, X. Tong, G. Sheng, Y. Shao, L. Yu, V. Tung, J. Sun, R.B. Kaner, Z. Liu, Printable magnesium ion quasi-solid-state asymmetric supercapacitors for flexible solar-charging integrated units, Nat. Commun. 10 (2019) 4913, https://doi.org/10.1038/s41467-019-12900-4.

[11] C. Li, S. Cong, Z. Tian, Y. Song, L. Yu, C. Lu, Y. Shao, J. Li, G. Zou, M.H. Rümmeli, S. Dou, J. Sun, Z. Liu, Flexible perovskite solar cell-driven photo-rechargeable lithium-ion capacitor for self-powered wearable strain sensors, Nano Energy 60 (2019) 247–256, https://doi.org/10.1016/j.nanoen.2019.03.061.

[12] Z. Tian, Z. Sun, Y. Shao, L. Gao, R. Huang, Y. Shao, R.B. Kaner, J. Sun, Ultrafast rechargeable Zn micro-batteries endowing wearable solar charging system with high overall efficiency, Energy Environ. Sci. 14 (2021) 1602–1611, https://doi.org/10.1039/D0EE03623D.

[13] A. Gurung, K. Chen, R. Khan, S.S. Abdulkarim, G. Varnekar, R. Pathak, R. Naderi, Q. Qiao, Highly efficient perovskite solar cell photocharging of lithium ion battery using DC–DC booster, Adv. Energy Mater. 7 (2017) 1602105, https://doi.org/10.1002/aenm.201602105.

[14] Z. Chen, J.W. To, C. Wang, Z. Lu, N. Liu, A. Chortos, L. Pan, F. Wei, Y. Cui, Z. Bao, A three-dimensionally interconnected carbon nanotube–conducting polymer hydrogel network for high-performance flexible battery electrodes, Adv. Energy Mater. 4 (2014) 1400207, https://doi.org/10.1002/aenm.201400207.

[15] J. Ren, Y. Zhang, W. Bai, X. Chen, Z. Zhang, X. Fang, W. Weng, Y. Wang, H. Peng, Elastic and wearable wire-shaped lithium-ion battery with high electrochemical performance, Angew. Chem. 126 (2014) 7998–8003, https://doi.org/10.1002/ange.201402388.

[16] T. Yang, D. Xie, Z. Li, H. Zhu, Recent advances in wearable tactile sensors: materials, sensing mechanisms, and device performance, Mater. Sci. Eng. R Rep. 115 (2017) 1–37, https://doi.org/10.1016/j.mser.2017.02.001.

[17] S. Liu, Z. Wang, C. Yu, H.B. Wu, G. Wang, Q. Dong, J. Qiu, A. Eychmüller, X. W. Lou, A flexible TiO2 (B)-based battery electrode with superior power rate and ultralong cycle life, Adv. Mater. 25 (2013) 3462–3467, https://doi.org/10.1002/adma.201300953.

[18] S. Xu, Y. Zhang, J. Cho, J. Lee, X. Huang, L. Jia, J.A. Fan, Y. Su, J. Su, H. Zhang, A. Stretchable batteries with self-similar serpentine interconnects and integrated wireless recharging systems, Nat. Commun. 4 (2013) 1–8, https://doi.org/10.1038/ncomms2553.

[19] Z. Zhang, X. Chen, P. Chen, G. Guan, L. Qiu, H. Lin, Z. Yang, W. Bai, Y. Luo, H. Peng, Integrated polymer solar cell and electrochemical supercapacitor in a flexible and stable fiber format, Adv. Mater. 26 (2014) 466–470, https://doi.org/10.1002/adma.201302951.

[20] N. Li, Y. Wang, D. Tang, H. Zhou, Integrating a photocatalyst into a hybrid lithium–sulfur battery for direct storage of solar energy, Angew. Chem. 127 (2015), https://doi.org/10.1002/anie.201503425, 9403, 9274.

[21] Y. Di, S. Jia, X. Yan, J. Liang, S. Hu, Available photo-charging integrated device constructed with dye-sensitized solar cells and lithium-ion battery, New J. Chem. 44 (2020) 791–796, https://doi.org/10.1039/C9NJ05367K.

[22] O.H. Kwon, J.H. Oh, B. Gu, M.S. Jo, S.H. Oh, Y.C. Kang, J.K. Kim, S.M. Jeong, J. S. Cho, Porous SnO2/C nanofiber anodes and LiFePO4/C nanofiber cathodes with a wrinkle structure for stretchable lithium polymer batteries with high electrochemical performance, Adv. Sci. 7 (2020) 2001358, https://doi.org/10.1002/advs.202070093.

[23] J. Mohanta, D.-W. Kang, J.S. Cho, S.M. Jeong, J.-K. Kim, Stretchable electrolytes for stretchable/flexible energy storage systems–Recent developments, Energy Storage Mater. 28 (2020) 315–324, https://doi.org/10.1016/j.ensm.2020.03.009.

[24] X. Wang, B. Liu, R. Liu, Q. Wang, X. Hou, D. Chen, R. Wang, G. Shen, Fiber-based flexible all-solid-state asymmetric supercapacitors for integrated photodetecting system, Angew. Chem. 126 (2014) 1880–1884, https://doi.org/10.1002/ange.201307581.

[25] S. Tan, N. Zhou, Y. Chen, L. Li, G. Liu, P. Liu, C. Zhu, J. Lu, W. Sun, Q. Chen, H. Zhou, Effect of high dipole moment cation on layered 2D organic–inorganic halide perovskite solar cells, Adv. Energy Mater. 9 (2019) 1803024, https://doi.org/10.1002/aenm.201803024.

[26] J.-K. Kim, J.-H. Ahn, P. Jacobsson, Influence of temperature on ionic liquid-based gel polymer electrolyte prepared by electrospun fibrous membrane, Electrochim. Acta 116 (2014) 321–325, https://doi.org/10.1016/j.electacta.2013.11.061.

[27] I. Mora-Sero, G. Garcia-Belmonte, P.P. Boix, M.A. Vazquez, J. Bisquert, Impedance spectroscopy characterisation of highly efficient silicon solar cells under different light illumination intensities, Energy Environ. Sci. 2 (2009) 678–686, https://doi.org/10.1039/B812468J.

[28] H.-J. Kim, G.-H. Bae, S.-M. Lee, J.-H. Ahn, J.-K. Kim, Properties of lithium iron phosphate prepared by biomass-derived carbon coating for flexible lithium ion batteries, Electrochim. Acta 300 (2019) 18–25, https://doi.org/10.1016/j.electacta.2019.01.057.

[29] I. Seo, B. Senthilkumar, K.-H. Kim, J.-K. Kim, Y. Kim, J.-H. Ahn, J. Atomic structural and electrochemical impact of Fe substitution on nano porous $LiMnPO_4$, J. Power Sources 320 (2016) 59–67, https://doi.org/10.1016/j.jpowsour.2016.04.061.

[30] J.-E. Lim, J. Kim, Y. Kim, J.-K. Kim, Binder-free hybrid Li4Ti5O12 anode for high performance lithium-ion batteries, Electrochim. Acta 282 (2018) 270–275, https://doi.org/10.1016/j.electacta.2018.06.057.

[31] X. Sun, P.V. Radovanovic, B. Cui, Advances in spinel Li 4 Ti 5 O 12 anode materials for lithium-ion batteries, New J. Chem. 39 (2015) 38–63, https://doi.org/10.1039/C4NJ01390E.

[32] C. Zhu, R.E. Usiskin, Y. Yu, J. Maier, The nanoscale circuitry of battery electrodes, Sci 358 (2017) 1, https://doi.org/10.1126/science.aao2808.

[33] J. Mohanta, H.-J. Kim, S.M. Jeong, J.S. Cho, H.-J. Ahn, J.-H. Ahn, J.-K. Kim, High-performance quasi-solid-state flexible sodium metal battery: substrate-free FeS2–C composite fibers cathode and polyimide film-stuck sodium metal anode, Chem. Eng. J. 391 (2020) 123510, https://doi.org/10.1016/j.cej.2019.123510.

[34] J.K. Kim, Electrode materials with a crater-type morphology prepared by electrospraying for high-performance lithium-ion batteries, ChemSusChem 12 (2019) 4487–4492, https://doi.org/10.1002/cssc.201901972.

[35] H. Yu, J.S. Han, G.C. Hwang, J.S. Cho, D.-W. Kang, J.-K. Kim, Optimization of high potential cathode materials and lithium conducting hybrid solid electrolyte for high-voltage all-solid-state batteries, Electrochim. Acta 365 (2021) 137349, https://doi.org/10.1016/j.electacta.2020.137349.

[36] N. Delaporte, G. Lajoie, S. Collin-Martin, K. Zaghib, Toward low-cost all-organic and biodegradable Li-ion batteries, Sci. Rep. 10 (2020) 1–18, https://doi.org/10.1038/s41598-020-60633-y.

[37] I. Seo, C.-R. Lee, J.-K. Kim, Zr doping effect with low-cost solid-state reaction method to synthesize submicron Li4Ti5O12 anode material, J. Phys. Chem. Solid. 108 (2017) 25–29, https://doi.org/10.1016/j.jpcs.2017.04.011.

[38] H.-D. Um, K.-H. Choi, I. Hwang, S.-H. Kim, K. Seo, S.-Y. Lee, Monolithically integrated, photo-rechargeable portable power sources based on miniaturized Si solar cells and printed solid-state lithium-ion batteries, Energy Environ. Sci. 10 (2017) 931–940, https://doi.org/10.1039/C6EE03266D.

[39] J. Kim, H. Park, J. Jang, H. Song, B.H. Lee, D. Lee, S. Jang, J.H. Kim, H.-J. Kim, Integrated energy conversion and storage device for stable fast charging power systems, ECS J. Solid State Sci. Technol. 9 (2020) 125003, https://doi.org/10.1149/2162-8777/abcc49.